Chinese Chemical Letters 36 (2025) 109765

Contents lists available at ScienceDirect

Chinese Chemical Letters

journal homepage: www.elsevier.com/locate/cclet

Strength through unity: Alkaline phosphatase-responsive AIEgen nanoprobe for aggregation-enhanced multi-mode imaging and photothermal therapy of metastatic prostate cancer

Ze Wang[a], Hao Liang[a], Annan Liu[a], Xingchen Li[a], Lin Guan[a], Lei Li[b], Liang He[c,*], Andrew K. Whittaker[d], Bai Yang[a], Quan Lin[a,*]

[a] State Key Laboratory of Supramolecular Structure and Materials, College of Chemistry, Jilin University, Changchun 130012, China
[b] Department of Endocrinology, Lequn Branch, the First Hospital of Jilin University, Changchun 130021, China
[c] Department of Urology, the First Hospital of Jilin University, Changchun 130021, China
[d] Australian Institute for Bioengineering and Nanotechnology, the University of Queensland, Brisbane, QLD 4072, Australia

ARTICLE INFO

Article history:
Received 11 January 2024
Revised 9 March 2024
Accepted 12 March 2024
Available online 12 March 2024

Keywords:
AIE
Prostate cancer
ALP responsive
Enhanced multi-mode imaging
Enhanced photothermal therapy

ABSTRACT

Prostate cancer (PCa) is characterized by high incidence and propensity for easy metastasis, presenting significant challenges in clinical diagnosis and treatment. Tumor microenvironment (TME)-responsive nanomaterials provide a promising prospect for imaging-guided precision therapy. Considering that tumor-derived alkaline phosphatase (ALP) is over-expressed in metastatic PCa, it makes a great chance to develop a theranostics system with ALP responsive in the TME. Herein, an ALP-responsive aggregation-induced emission luminogens (AIEgens) nanoprobe AMNF self-assembly was designed for enhancing the diagnosis and treatment of metastatic PCa. The nanoprobe exhibited self-aggregation in the presence of ALP resulted in aggregation-induced fluorescence, and enhanced accumulation and prolonged retention period at the tumor site. In terms of detection, the fluorescence (FL)/computed tomography (CT)/magnetic resonance (MR) multi-mode imaging effect of nanoprobe was significantly improved post-aggregation, enabling precise diagnosis through the amalgamation of multiple imaging modes. Enhanced CT/MR imaging can achieve assist preoperative tumor diagnosis, and enhanced FL imaging technology can achieve "intraoperative visual navigation", showing its potential application value in clinical tumor detection and surgical guidance. In terms of treatment, AMNF showed strong absorption in the near infrared region after aggregation, which improved the photothermal treatment effect. Overall, our work developed an effective aggregation-enhanced theranostic strategy for ALP-related cancers.

Prostate cancer (PCa) is a highly prevalent tumor of the male genitourinary system and one of the leading causes of cancer death in men worldwide [1,2]. Due to its bone-philicity, it is prone to bone metastasis. The precise diagnosis and treatment of metastatic PCa still face many clinical challenges. In terms of diagnosis, current clinical imaging techniques such as computed tomography (CT), magnetic resonance imaging (MRI), and choline positron emission tomography (PET) have been used to diagnose PCa and its metastases [3]. However, traditional contrast agents (such as iodine small-molecule) have high toxic and side effects, and are limited to single-mode imaging, which faces challenges such as insufficient resolution and sensitivity [4,5]. It is difficult to accurately determine the location of PCa, making surgery face great challenges. Fluorescence (FL) imaging is a promising imaging method that can be used for disease surveillance and guiding surgery. Many fluorescent probes have been successfully used for imaging biological tissues, such as carbon dots and down-conversion nanoparticles. Unfortunately, these fluorescent probes face the challenges of fluorescence bleaching, high toxicity, hydrophobicity, and low quantum yield when imaging *in vivo* [6]. In terms of treatment, the main treatment methods for metastatic PCa are androgen deprivation therapy (ADT) and chemotherapy. However, ADT often causes drug resistance, making PCa transform into castration-resistant PCa (CRPC), which seriously affects the quality of life of patients [7]. In addition, systemic toxicity and side effects hinder the further application of chemotherapy [8]. In conclusion, it is of great clinical significance to design a theranostic platform that can accurately diagnose and treat PCa with bone metastases.

* Corresponding authors.
E-mail addresses: lianghe9278@jlu.edu.cn (L. He), linquan@jlu.edu.cn (Q. Lin).

https://doi.org/10.1016/j.cclet.2024.109765
1001-8417/

In recent years, nanomaterials have been widely used in the biomedical field including biosensing, biomedicine, diagnostic imaging and oncotherapy. In particular, gold nanoparticles (AuNPs) have attracted much attention from researchers due to their excellent fluorescence properties, biocompatibility, and ease of surface functionalization [9–13]. Manganese (Mn) is an essential trace element for maintaining human physiological functions, while Mn^{2+} is a paramagnetic metal ion with promising MRI effect and widely used in biomedicine [14,15]. Based on the advantages of AuNPs and Mn^{2+}, developing an effective and simple method to assemble AuNPs and Mn^{2+} into a single multifunctional spherical nanoparticle can better exert their advantages in tumor diagnosis and treatment. Notably, the antitumor effect of gold-based nanomaterials is closely related to their size. The smaller AuNPs (<20 nm) have better fluorescence properties, deeper tissue penetration, and more uniform diffusion within the tumor tissue [16–18]. Unfortunately, they are easily excreted by the body, resulting in insufficient tumor accumulation, making diagnostic and therapeutic efficacy limited [19]. Larger AuNPs (>100 nm) can exert enhanced permeability and penetration (EPR) effects and generally exhibit strong absorption in the near infrared (NIR) region, making them suitable for photothermal therapy (PTT) [20,21]. However, they are easily captured by the reticuloendothelial system (RES), leading to unsatisfactory treatment outcomes [22]. To resolve the above contradictions, stimulus-induced size aggregation systems may provide a solution while taking full advantage of nanoparticles.

To date, researchers have developed a number of techniques to induce nanoparticle aggregation, such as external stimuli (temperature, light, electric and magnetic fields, *etc.*) or the tumor microenvironment (TME, pH, redox species, *etc.*) [23]. Recently, researchers have found that self-assembly of nanoparticles can also be effectively triggered by enzymes that are overexpressed in TME, along with the aggregation-induced emission (AIE) phenomenon [24–26]. Alkaline phosphatase (ALP) has been reported to be overexpressed on the membrane structures of certain tumors, such as liver cancer, cervical cancer, osteosarcoma, and especially advanced PCa with bone metastasis [27–29]. It has become an important biomarker for targeted imaging, diagnosis, and therapy of related cancers. ALP is characterized by dephosphorylation effect on its substrates to produce more hydrophobic products, along with self-assembly (or aggregation) of products [30]. Therefore, the development of an ALP-triggered aggregation of gold-based nanomaterials at the tumor site may be a novel and effective strategy for improving the diagnostic accuracy and therapeutic efficacy of metastatic PCa in clinic.

Inspired by the strategy of enzyme-mediated nanoparticle aggregation *in situ*, we designed ALP-triggered AIEgen nanoprobe self-assembly for aggregation-enhanced multi-mode imaging and PTT of metastatic PCa (Scheme 1). Firstly, Au/Mn nanodots (AMN) with excellent biocompatibility, multi-mode imaging and PTT function were prepared. Then, AMN combined with ALP-responsive peptide (Phe-Phe-Tyr(H_2PO_3)-OH, designated as FTp) to form AMN-FTp (AMNF) through amidation. In ALP-positive tumor tissues (such as metastatic PCa), after ALP-catalyzed dephosphorylation, the products can self-assemble through intermolecular interactions (*e.g.*, intermolecular H-bonds, hydrophobic interactions and $\pi-\pi$ stacking) due to the strong hydrophobic effect of benzene ring exposure, showing significant aggregation at the tumor site [27,31,32]. TME-responsive *in situ* aggregation of nanoprobe may have three obvious advantages: (1) Increasing the concentration and retention time of the nanodots (NDs) at the tumor site. (2) The multi-mode imaging effect (FL/CT/MR) can be significantly improved after aggregation, and the accurate diagnosis of PCa and its metastases can be achieved by combining multiple imaging modalities. In addition, enhanced FL imaging can realize "intraoperative visualization navigation" and provide good guidance for clinical surgery. (3) After aggregation, AMNF has a strong absorption in the NIR region to further improve the PTT effect.

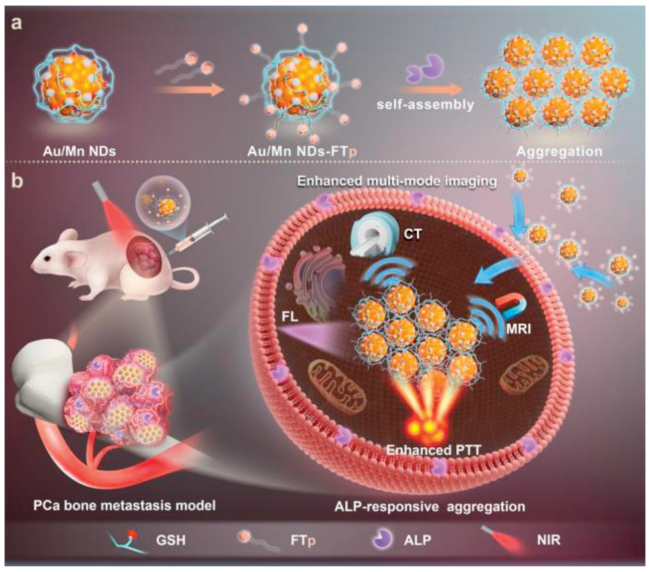

Scheme 1. Schematic illustration of (a) preparation and ALP-triggered self-assembly of AMNF nano-system, and (b) used for enhanced multi-mode imaging and photothermal therapy of metastatic prostate cancer.

The ALP-triggered self-assembly of AMNF nano-system were synthesized for enhanced multi-mode imaging and PTT of metastatic PCa, as shown in Scheme 1. Firstly, the AMN with ultrasmall size and good biocompatibility were synthesized by electrochemical exchange method. It can be seen from the transmission electron microscopy (TEM) images that the morphology of AMN is spherical and the size was about 4.6 nm (Fig. S1a in Supporting information). The hydration particle size of the solution of AMN was about 27.25 nm, which was slightly larger than the size measured by TEM in the dry state (Fig. S1b in Supporting information). The fluorescence property of AMN was investigated. As shown in Fig. S2 (Supporting information), AMN displayed a strong emission peak at 376 nm excitation. The magnetic responsiveness of AMNF was investigated (Fig. S3 in Supporting information). The magnetization curve showed that the AMN have a good superparamagnetism (magnetic coercivity at 298 K is close to 0 Oe). Superparamagnetism is beneficial for MRI *in vivo*, which can not only reduce the energy loss, but also keep the imaging intensity stable. Furthermore, the chemical composition and elemental valence states of AMN was assessed by X-ray photoelectron spectroscopy (XPS). XPS survey spectrum of AMN contains characteristic peaks of Au 4f, Mn 2p, S 2p, O 1s and C 1s (Fig. S4 in Supporting information). As shown in Fig. S5 in Supporting information, the Au 4f peaks at 88.80 and 85.05 eV indicate the coexistence of Au(0) and Au(I) [33]. Au(0) is conducive to the nucleation of nanodots. Au(I) can react with the sulfhydryl group of the ligand to form Au-S bond, which not only gives nanodots the bright and stable fluorescence characteristics, but also enhances the stability. The Mn 2p peaks at 653.80 and 642.40 eV were assigned to Mn^{2+}, which provides the possibility for MRI *in vivo* (Fig. S6 in Supporting information) [34]. The characteristic peaks at 163.50 and 164.60 eV were attributed to S 2p (Fig. S7 in Supporting information). Thus, AMN with ultra-small size, excellent fluorescence and magnetic properties were synthesized.

To achieve the strategy of enzyme-induced nanoparticle aggregation *in situ*, ALP-responsive nanoprobe AMNF was synthesized by connecting AMN with the ALP-sensitized peptides (FTp) through amide bond. The zeta potential of the AMNF was investigated by

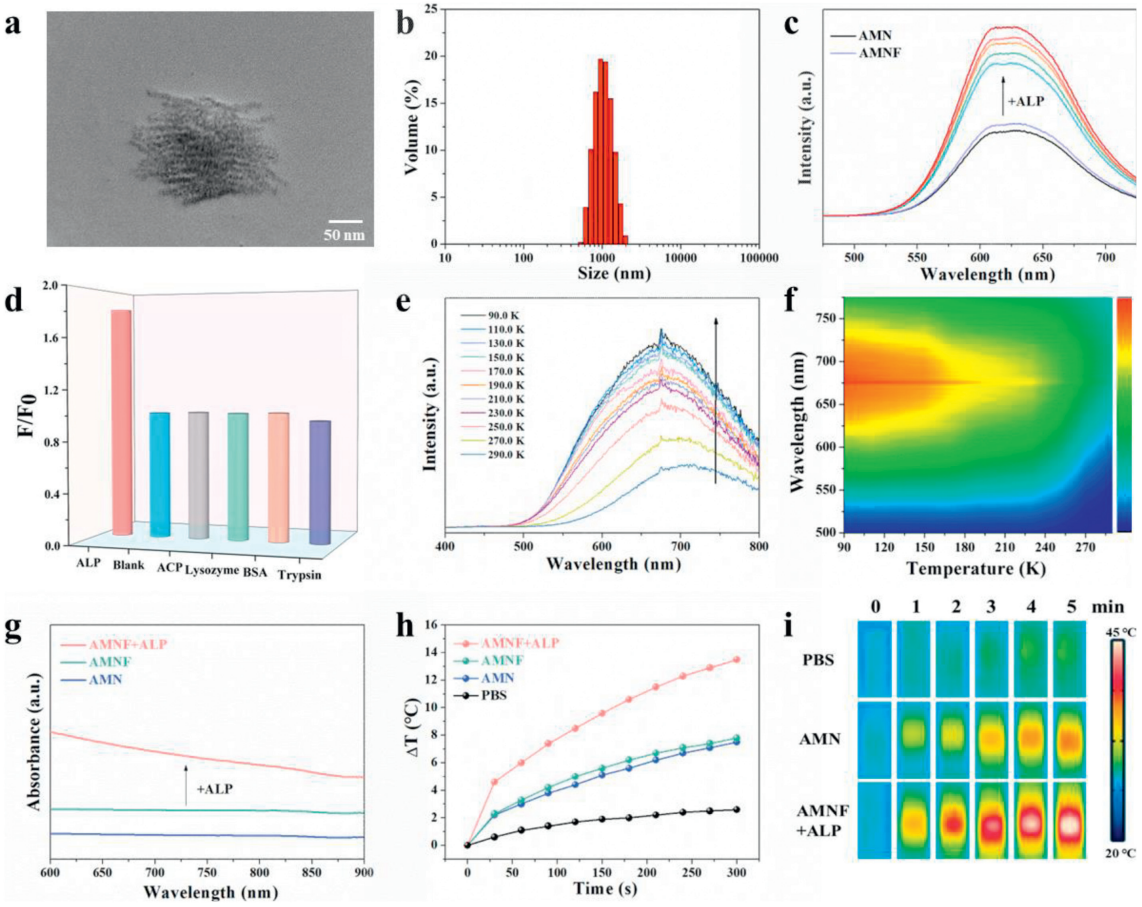

Fig. 1. ALP-mediated self-assembly of AMNF. (a) TEM image and (b) hydration particle size distribution of the AMNF after the addition of ALP (30 U/mL, 37 °C) for 2 h. (c) Fluorescence spectra of AMN, and AMNF following incubation with varying concentration (0, 10, 20, 30, 40 and 50 U/mL, 37 °C) of ALP for 2 h. (d) Fluorescence intensity of AMNF incubated with trypsin, BSA, lysozyme, ACP or ALP. (e, f) Temperature-dependent photoluminescence emission spectra of AMNF after the addition of ALP under 376 nm excitation. (g) UV spectra of AMN, AMNF and AMNF + ALP. (h) Temperature change of the PBS (as control), AMN, AMNF and AMNF + ALP solution under the 808 nm laser irradiation as a function of irradiation time. (i) Infrared thermal images of PBS (as control), AMN and AMNF + ALP solution under the 808 nm laser irradiation as a function of irradiation time.

dynamic light scattering (DLS) (Fig. S8 in Supporting information). AMN had a large negative charge (-30.4 ± 2.61 mV), while AMNF was close to neutral (-7.11 ± 0.94 mV) when connected to positively charged FTp ($+6.94 \pm 3.58$ mV), indicating that the surface potential of AMNF was partially neutralized. As shown in the infrared spectrogram, there was no characteristic peak of AMN at 785 cm^{-1}, the characteristic peak of benzene appeared in both FTp and AMNF at the same position. Meanwhile, FTp and AMNF showed characteristic peaks at 1016–1223 cm^{-1}, which may be attributed to the P=O and P–O bond stretching vibration peaks of FTp (Fig. S9 in Supporting information). These results indicate that AMN and FTp are successfully connected. The spectra of proton nuclear magnetic resonance (^{1}H NMR) were demonstrated in Fig. S10 (Supporting information). The presence of resonances at 7.13 ppm was attributed to the characteristic peak of benzene of FTp. The characteristic peak of benzene also presented at the same position of AMNF. These results supported the formation of the stable structure of AMNF.

The ALP-mediated self-assembly of AMNF was evaluated *in vitro*. After ALP-catalyzed dephosphorylation, the exposed benzene ring of the products has a strong hydrophobic effect, and AMNF can achieve self-aggregation through efficient intermolecular interactions (*e.g.*, intermolecular H-bonds, hydrophobic interactions and $\pi-\pi$ stacking) [27,31]. It can be seen directly from the TEM images that after adding ALP, the size of aggregate particle is about 165 nm, indicating that there is self-assembly among nanoparticles happened in the presence of ALP (Fig. 1a). The self-assembling behavior of AMNF was further evaluated through DLS. Upon ALP treatment, the hydration particle size of AMNF was increased to 1069 nm (Fig. 1b). In addition, after ALP-catalyzed dephosphorylation, the solution of AMNF gradually changed from clear to cloudy, which could be recognized with the naked eye (Fig. S11 in Supporting information). These results supported that the enzyme-mediated self-assembly of AMNF took place. Next, the responsiveness of AMNF to ALP was detected by fluorescence spectroscopy. As shown in Fig. 1c, the fluorescence intensity increases with the increase of ALP concentration, indicating that AMNF has a good responsiveness to ALP. There is a good linear relationship between the fluorescence intensity centered at wavelength of 624 nm and ALP concentrations ($R^2 = 0.988$, Fig. S12 in Supporting information). A subsequent test of AMNF selectivity toward ALP over other representative enzymes (*e.g.*, trypsin, BSA, lysozyme, acid phosphatase (ACP)) showed that only ALP could show a significant enhancement of the fluorescent signal (Fig. 1d). This suggests that AMNF has the potential to be used as an ALP-specific biosensor for monitoring ALP activity in complex biological samples.

In 2001, Tang's group puts forward the concept of AIE, describing an abnormal phenomenon that weak fluorescence or even no fluorescence in solution but strong emission once aggregated, which is opposite to the aggregation-caused quenching (ACQ) effect [35–38]. When the nanodots gather, the molecular conformation is highly distorted and the intramolecular motion is re-

stricted, regulating the energy release of the excited state, leading to brighter fluorescence. Therefore, we support that "restricted intramolecular motion (RIM)" is the main cause of AIE phenomenon. To test this hypothesis, we restricted intramolecular motion by changing the external environment (decreasing the temperature). We studied emission behavior of AMNF + ALP at low temperatures, at which their intramolecular motion will be strongly suppressed (Figs. 1e and f). The results showed that the fluorescence intensity of AMNF + ALP increased gradually as the temperature decreased from 290 K to 90 K. In the absence of ALP, the fluorescence intensity of AMNF did not change with the decrease of temperature (Fig. S13 in Supporting information). In summary, the intramolecular rotation of AMNF + ALP is strongly inhibited at low temperature, resulting in enhanced fluorescence, which is consistent with the properties of AIE.

To verify the responsiveness of AMNF to ALP, the visible-NIR spectrum was detected. As shown in Fig. 1g, the absorption of AMNF + ALP was obviously higher than that of AMN and AMNF, indicating that AMNF has more potential for PTT in the presence of ALP. Then, photothermal properties were evaluated. As shown in Fig. 1h, under the irradiation of 808 nm laser at 2.0 W/cm^2, temperature raise of AMNF + ALP was faster and higher (the maximum temperature raise, $\Delta T_{max} = 13.5$ °C) at each point in time than that of AMNF ($\Delta T_{max} = 7.8$ °C) and AMN ($\Delta T_{max} = 7.5$ °C). The temperature increases of the phosphate buffered saline (PBS; as control) was negligible. The temperature changes between the different groups can also be more intuitively observed with infrared thermal images (Fig. 1i). The above results strongly confirm that the ALP-indicated aggregation of AMNF enhances the photothermal properties, which can be used as the potential photothermal agent (PTA) for PTT.

Good biocompatibility is the foundation for further applications of nanomaterials. Therefore, we applied the Cell Counting Kit 8 (CCK8) method to evaluate the biocompatibility of the AMNF. Different concentration of AMN and AMNF (0, 12.5, 25, 50, 100, and 200 μg/mL) were co-cultured with PC-3 and MCF-7 cells for 24 h (Figs. 2a and b) and 48 h (Fig. S14 in Supporting information). As shown in the figures, even at the highest concentration (200 μg/mL), the cell viability of PC-3 and MCF-7 can still be maintained at over 80%. Moreover, with the extension of co-culture time, the cells survival rate was still above 80% (Figs. S14a and b). These results indicating that AMNF have good biocompatibility.

Then, we conducted *in vitro* cell experiments to validate the ALP-responsive characteristics, the binding ability and localization of AMNF with tumor cells. Initially, we utilized flow cytometry to assess the fluorescence intensity of PC-3 and MCF-7 cells after 12 h of co-culturing with AMN and AMNF, respectively (Figs. 2d and e). When PC-3 cells were co-cultured with AMNF, the average fluorescence intensity was significantly increased compared to AMN. However, the average fluorescence intensity of ALP negative MCF-7 cells co-cultured with AMNF or AMN had no significant difference (Fig. 2c). The results indicated that the AMNF can be stimulated to aggregate by highly expressed ALP in PC-3 cells, thereby inducing intense fluorescence intensity.

Based on flow cytometry results, we used confocal microscopy to visually observe the aggregation of AMNF in cells. The confocal microscopy results showed that the fluorescence signal of AMNF group was obvious in PC-3 cells, and the fluorescence intensity of PC-3 cells with AMNF was 2.93-fold compared with AMN (Figs. 2f and g). On the contrary, there was no significant difference in fluorescence intensity between AMNF and AMN in MCF-7 cells (Figs. 2h and i). Both of flow cytometry and confocal microscopy results confirmed that AMNF significantly aggregated in PC-3 cells, increasing the concentration of intracellular nanoparticles. Furthermore, the enhanced fluorescence intensity suggests that it can be used as an excellent fluorescence probe for the diagnosis of ALP-related tumors.

For advanced PCa, particularly metastatic PCa, where surgery is not suitable, conservative treatment modalities such as ADT and chemotherapy play a crucial role. However, ADT often leads to the development of resistance, resulting in the transition of PCa to castration-resistant prostate cancer (CRPC). Chemotherapy can potentially cause severe side effects and systematic toxicity. PTT is a recently developed cancer treatment modality that utilizes PTAs to convert near-infrared light into heat, effectively ablating tumors. In comparison to traditional advanced PCa therapies, PTT exhibits significant advantages in terms of precise spatial-temporal positioning and reduced invasiveness. To study the effect of PTT *in vitro*, CCK8 assay was applied (Fig. 2j). After laser irradiation for 1, 3 and 5 min, PC-3 cells viability of AMNF and AMN groups decreased significantly. This result indicates that gold-based nanomaterials have the potential for clinical PTT. Notably, AMNF exhibited greater cytotoxicity compared to AMN under the same photothermal conditions. This may be due to the fact that in PC-3 cells, AMNF showed significant aggregation, which further enhanced the PTT effect. Enhanced PTT effect simultaneously induces morphological of PC-3 cells changes (Fig. S15 in Supporting information), exhibiting significantly signs of apoptosis and excellent *in vitro* therapeutic effects.

To further improve the imaging and diagnostic accuracy of metastatic PCa, the ALP-responsive multi-mode imaging probe AMNF was designed. First, the FL imaging performance was evaluated *in vitro*. After the addition of ALP, the fluorescence emission intensity of AMNF increased by about 1.9 times (Fig. 3a). The difference of fluorescence intensity before and after aggregation can be visually seen from fluorescence images (Fig. 3b). Meanwhile, CT signals were also gradually enhanced after different concentrations (50, 100, 150 and 200 μg/mL) of AMNF incubation with ALP, which were higher than that of AMN at the same concentration (Fig. 3c). The CT signal value and image brightness are proportional to the concentration, so the enrichment degree of AMNF can be quantitatively analyzed according to the imaging effect (Fig. 3d). In addition, after the addition of ALP, the MR signal intensity of different concentrations of AMNF also increased, and was higher than that of the same concentration of AMN (Fig. 3e). This may be attributed to the fact that after the aggregation of AMNF triggered by ALP, the T_1 of water protons is gradually shortened due to the change of particle size, thus producing brighter T_1-weighted MR images (Fig. 3f).

After confirming the ALP sensitivity of AMNF through *in vitro* experiments, we further conducted research on its ALP-responsive multi-mode imaging (FL/CT/MRI) in PCa tibial metastasis xenografted mice. All animal experiments were approved by the Ethics Commission on Animal Use at Jilin University First Hospital. FL images showed that the fluorescence signal intensity of PCa bone metastasis site in the AMNF group gradually increased over time and reached a peak at 3 h after injection (Fig. 3g and Fig. S16 in Supporting information). The region of the fluorescence signal was also expanded, and the whole tumor was lit up at 3 h. The contrast between the tumor and the surrounding normal tissue was obvious, showing a clear tumor border. On the contrary, AMN showed a weaker FL signal in tumor tissues, and the fluorescence signal gradually diminishes after injection. These findings suggested that AMNF can achieve efficient aggregation and retention at the tumor site. The great FL imaging effect of AMNF achieved in this study holds the potential for "intraoperative detection" and can serve as a valuable guidance tool for clinical surgical procedures. Subsequently, the fluorescence distribution in resected organs and tumors was observed in the different groups. The results showed that the tumors of the "aggregate" group of

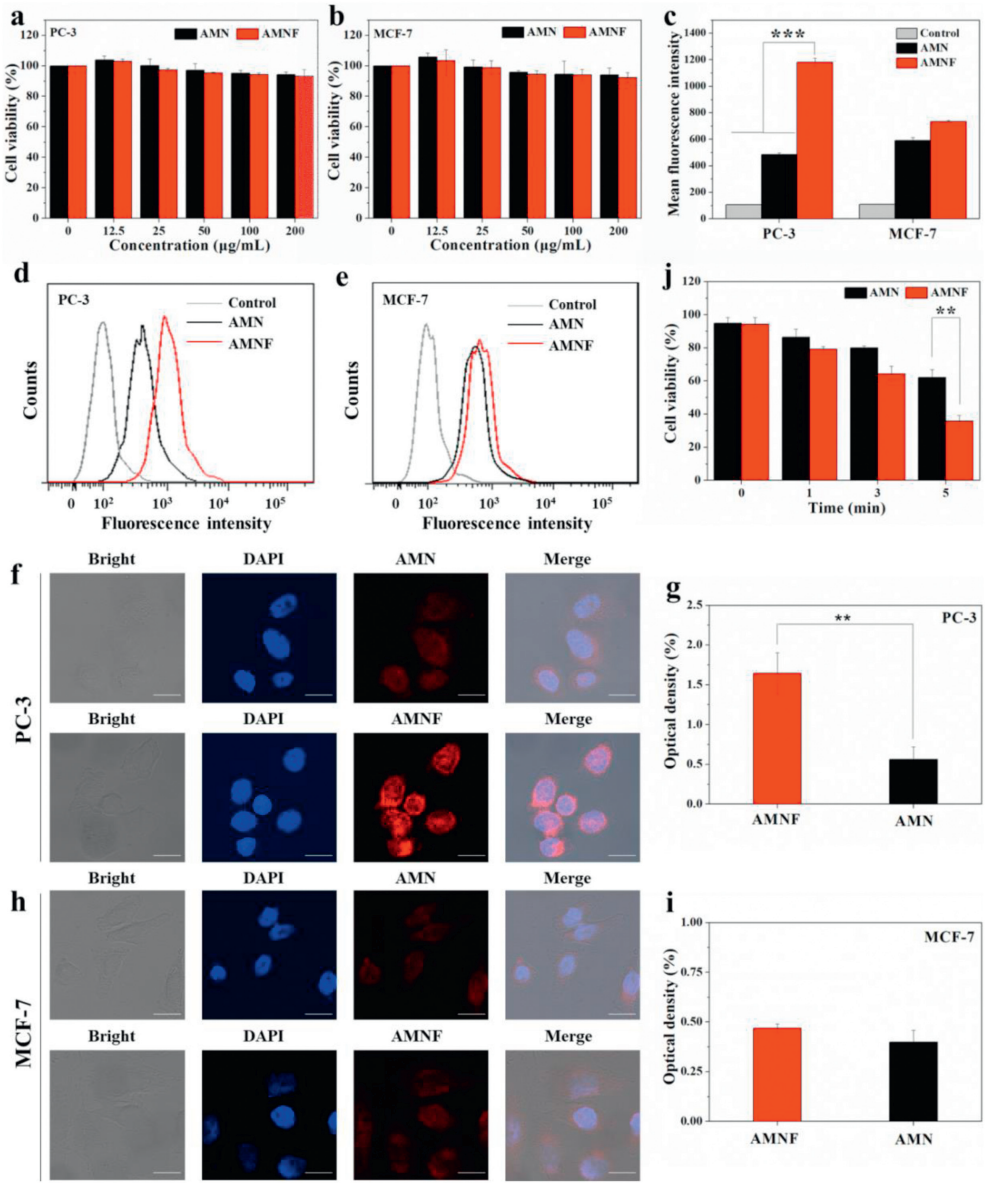

Fig. 2. Biocompatibility, ALP-responsive and photothermal ability of the AMNF *in vitro*. Effect of AMN, AMNF on (a) PC-3 and (b) MCF-7 cells viability at different concentrations for 24 h. (c) Quantitative analysis of fluorescence intensity of flow cytometry. Flow cytometry analysis of fluorecence intensity for (d) PC-3 and (e) MCF-7 cells incubated with AMN or AMNF. Confocal fluorescence images and semi-quantitative optical density for the localization of AMN or AMNF in (f, g) PC-3 and (h, i) MCF-7 cells. Scale bar: 20 μm. (j) Cell viability of PC-3 cells incubated with AMN or AMNF after irradiation with an 808 nm (2.0 W/cm^2) laser irradiation for 0, 1, 3 and 5 min. The data exhibited as mean ± SD ($n = 3$). $^{**}P < 0.01$, $^{***}P < 0.001$.

mice showed significantly higher fluorescence (Fig. S17 in Supporting information).

Then, to explore the possibility of AMNF as contrast agent, we evaluated CT/MR imaging efficacy of AMNF in PCa bone metastasis model. As shown in Fig. 3h, the CT imaging results demonstrated the enhancement in brightness after injection of both AMN and AMNF. However, the difference lies in the fact that CT enhancement caused by AMNF increased over time and could be sustained for a longer duration than AMN. CT intensity of AMN group exhibited a continuous decreasing after injection, whereas AMNF peaked at 3 h after injection (Fig. S18 in Supporting information). This result may be attributed to the ability of ALP in the PCa bone metastasis to induce the aggregation of AMNF, thereby prolonging their retention time at the tumor site. As for MRI detection, we confirmed that injection of AMN and AMNF can achieve enhancement in MRI within the bone metastatic lesions of PCa (Fig. 3i). Similar to the CT results, from the brightness perspective of MRI, AMNF demonstrates a stronger enhancement effect compared to AMN.

Taken together, supramolecular self-assembly of nanoparticles successfully occurred *in vivo* through our novel strategy of *in situ* inducing of nanoparticle aggregation based on ALP. The aggregation of nanoparticles not only reduces spread and prolongs their retention time, but also achieves enhanced FL/CT/MR multi-mode imaging effect. With the ability of aggregation *in situ* and enhanced multi-mode imaging effect, the AMNF nano-system provides precise localization of PCa bone metastasis. This unique capability empowers surgeons to identify lesion locations both preoperatively and during surgery, thereby enhancing the accuracy of PCa imaging prior to the procedure and guiding intraoperative resection. By harnessing the complementary strengths of each imaging modality, the AMNF nano-system exhibits its potential for clinical applica-

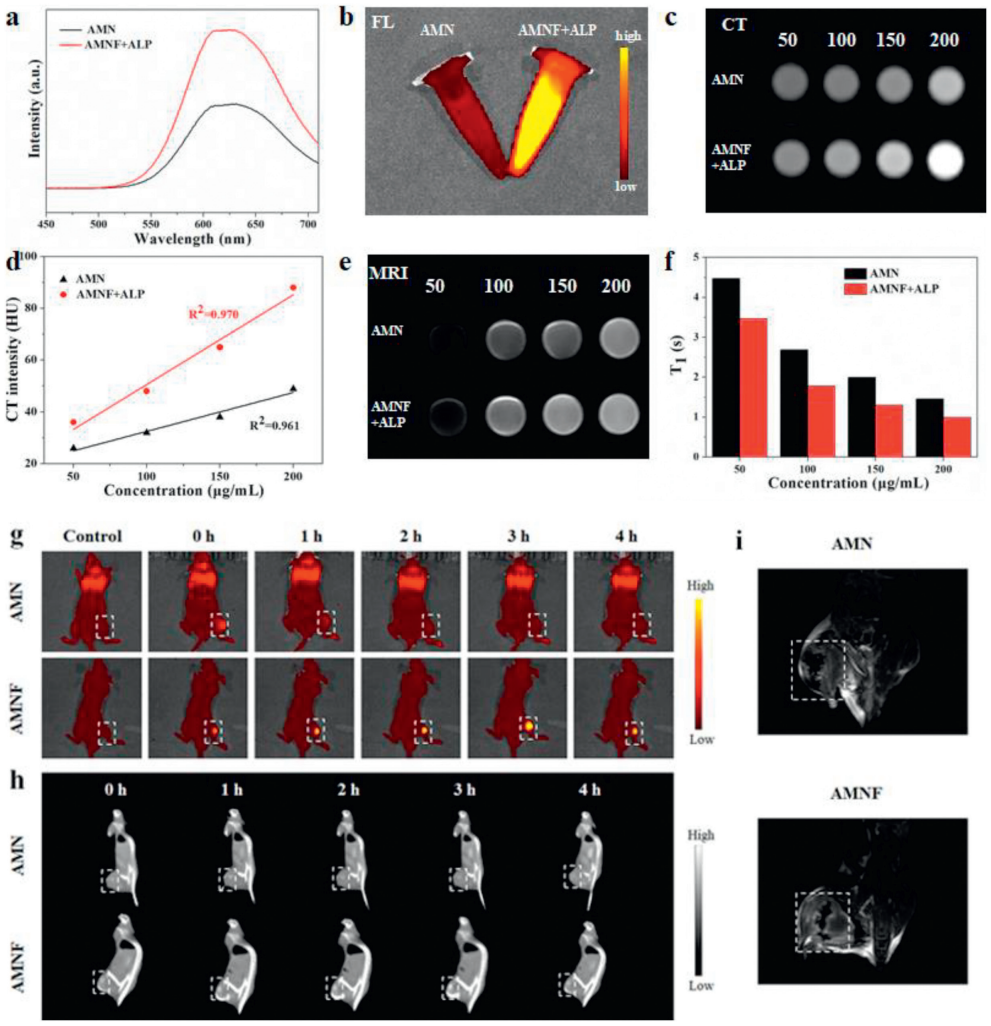

Fig. 3. ALP-triggered enhancing FL/CT/MR imaging of the nanoprobe AMNF *in vitro/in vivo*. (a) Fluorescence spectra and (b) fluorescence images of AMN and AMNF incubated with the ALP (30 U/mL, 37 °C) for 2 h. (c) CT images and (d) CT intensity trend of different concentrations (50, 100, 150 and 200 μg/mL) of AMN and AMNF incubated with the ALP (30 U/mL, 37 °C) for 2 h. (e) T_1-weighted MR images and (f) T_1 values of different concentrations (50, 100, 150 and 200 μg/mL) of AMN and AMNF incubated with the ALP (30 U/mL, 37 °C) for 2 h. (g) FL and (h) CT imaging of mice bearing PC-3 tumors injected with AMN or AMNF at different time points. (i) MR imaging of mice bearing PC-3 tumors injected with AMN or AMNF at 3 h. Tumors were circled with dashed lines.

tions in cancer detection and surgical guidance, offering promising prospects in the field of oncology.

In this study, we employed AMNF for PTT in PC-3 bone metastasis xenograft models (Fig. 4a). After the model of PCa tibial metastasis was established, the mice were randomly divided into six groups: Control, NIR, AMN, AMN + NIR, AMNF and AMNF + NIR. To monitor the spatial temperature distribution and temperature evolvement of the tumor in real time, temperature changes were continuously monitored using an infrared thermal imaging camera (Fig. 4b). After 5 min of 808 nm laser irradiation at 2.0 W/cm², the temperature at the tumor site in both AMN and AMNF group rapidly increased. Meanwhile, the temperature changes in the PBS group were not significant. Importantly, temperature raise of AMNF was faster and higher (the maximum temperature approximately 55 °C) at each point in time than AMN. This may be due to the aggregation of AMNF induced by the ALP *in vivo*, thereby enhancing its photothermal effect. Based on the potential for PTT of the AMNF nano-system, different groups of mice were treated. As shown in Fig. 4c, the PCa bone metastasis-growth in AMNF + NIR group was slower than that in other groups. Significantly, our findings revealed that the tumor volume observed in the AMNF + NIR group exhibited a notable reduction compared to the AMN + NIR group (Fig. 4c and Fig. S19 in Supporting information), consistent with the *in vitro* data.

After administering various treatments, hematoxylin and eosin (H&E), immunohistochemistry and immunofluorescence staining of tumor sections were performed to provide additional evidence of the therapeutic effect of the nano-system on metastatic PCa (Fig. 4e). The H&E staining results indicated that both AMN + NIR and AMNF + NIR groups have caused certain cytotoxic effects on tumor tissues. This could be attributed to photothermal ablation based on gold-nanomaterials. However, what differs is that the tumor apoptosis area is significantly higher in the AMNF + NIR group (65.80% ± 3.42%) compared to the AMN + NIR group (53.80% ± 1.64%) (Fig. 4f). This result could be due to the enhanced PTT effect of PCa after the aggregation of AMNF. Subsequently, different groups of tumor tissues were collected for immunohistochemical staining (caspase-3 and Ki67), as well as immunofluorescence staining terminal deoxynucleotidyl transferase-mediated dUTP nick-end labeling (TUNEL). Caspase-3 is a crucial enzyme that plays a vital role in the process of cell apoptosis. The quantitative analysis of caspase-3 staining revealed that AMNF + NIR group exhibited the highest abundance of positively stained cells (90.6% ± 2.30%) (Fig. 4h). TUNEL

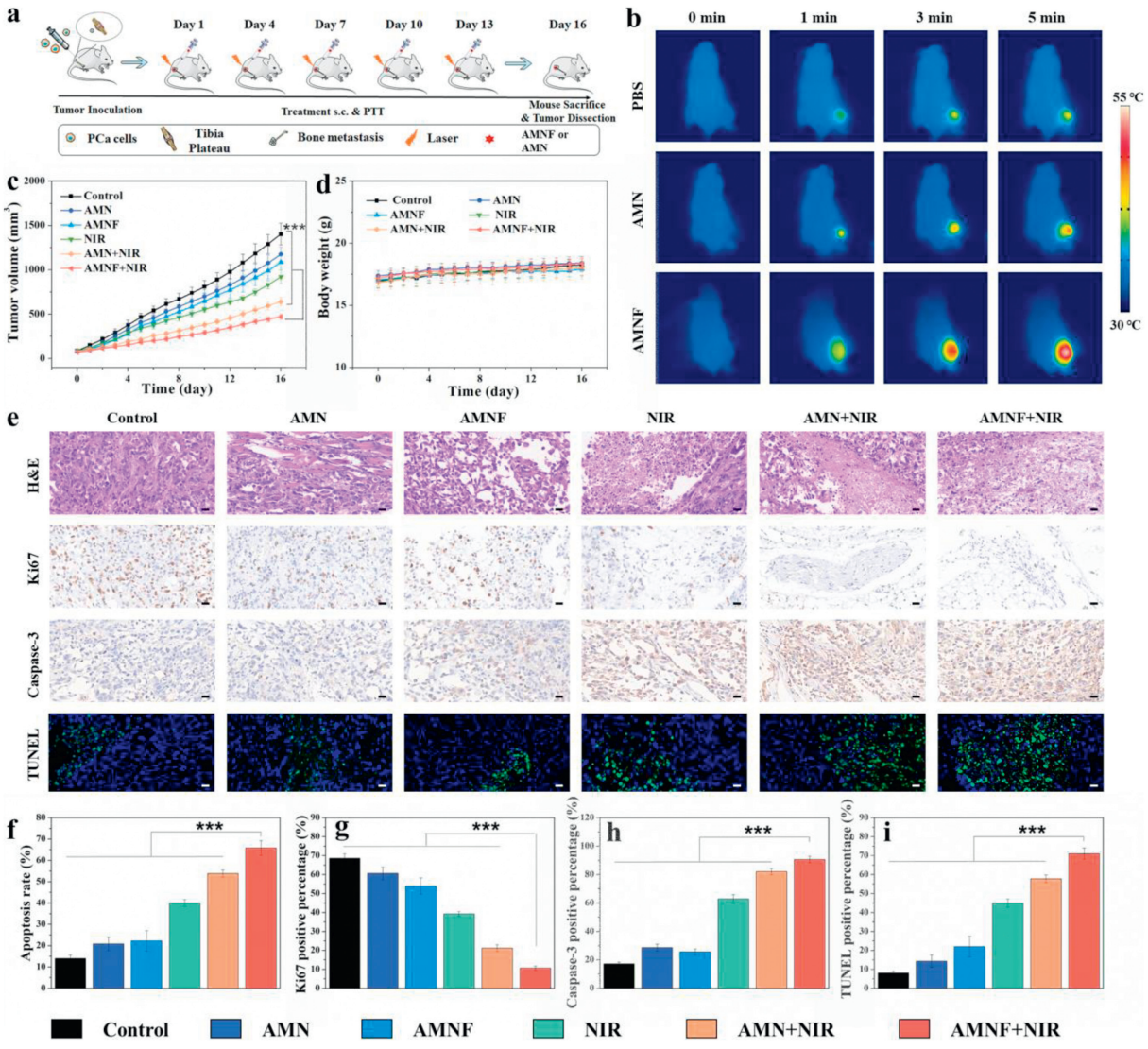

Fig. 4. Photothermal therapy effect *in vivo* and detection of PCa proliferation and apoptosis after therapy. (a) Schematic diagram showing the establishment of tibial metastasis model and treatment regimen. (b) Photothermal images of mice after injection of PBS, AMN or AMNF under 808 nm laser irradiation for 0, 1, 3 and 5 min. (c) Tumor volume and (d) body weight collected from mice with different treatment groups. (e) H&E staining of tumor sections after different treatments; immunohistochemistry staining of the caspase-3 and Ki67, immunofluorescence staining of TUNEL of the tumor tissues on the 16th day after different treatments. Scale bar: 20 μm. Quantitative analysis of the (f) tumor cell apoptosis, (g) Ki67-positive cells, (h) caspase-3 positive cells and (i) TUNEL-positive cells in tumor sections after different treatments. The data exhibited as mean ± SD ($n = 5$). $^{***}P < 0.001$.

is method widely used to detect apoptotic cells. In this work, we performed TUNEL staining and conducted quantitative analysis (Figs. 4e and i). The quantitative analysis of TUNEL positive area in AMNF + NIR group (71.02% ± 3.03%) was much higher than that in other groups, such as Control (8.04% ± 0.90%), AMN (14.28% ± 3.25%), AMNF (21.94% ± 5.47%), NIR (44.92% ± 2.20%), and AMN + NIR (57.76% ± 2.02%). This observation strongly suggests that the AMNF + NIR group achieved the highest level of tumor cell apoptosis among the experimental groups. Ki67 is an indicator of tumor proliferation. The results showed that the tumor sections from the AMNF + NIR group had lowest level of Ki67 protein content (Fig. 4e). Furthermore, quantitative analysis of Ki67 positive staining cells showed that AMNF + NIR group (10.6% ± 1.14%) was significantly lower than that of other groups (Fig. 4g). Overall, these results further confirmed that high ALP environment within the PCa region can induce the aggregation of AMNF, thereby enabling enhanced PTT capabilities upon laser irradiation.

Toxicity to the organism is also one of the important aspects considered when evaluating the application of nanomaterials. The body weight change is one of the primary indicators of organism intoxication. As shown in Fig. 4d, the weight changes among the various experimental groups of tumor-bearing mice did not exhibit any significant differences. Furthermore, on the 16th day, histological analysis of major organs was conducted to provide further confirmation regarding the biosafety of the nano-system (Fig. S20 in Supporting information). H&E staining of the heart, liver, spleen, lung and kidney in all treatment groups revealed no discernible signs of organ damage or abnormalities. This observation indicates the absence of systemic or chronic toxicity of AMNF nano-system.

In summary, based on enzyme-mediated self-assembly strategy, we prepared an ALP-responsive AIEgen AMNF for aggregation-enhanced diagnostic and therapeutic efficacy of metastatic PCa. Upon dephosphorylation in the presence of ALP, AMNF self-assembles into large aggregates. After aggregation, AMNF achieved high accumulation and prolonged retention time at the tumor

site. The results of *in vivo* and *in vitro* experiments showed that AMNF can significantly improve the FL/CT/MR multi-mode imaging effect after aggregation, and realize the accurate diagnosis of metastatic PCa. In addition, the absorption of AMNF was significantly enhanced after aggregation, further improving the effect of PTT *in vitro/in vivo*. It is anticipated that the enzyme-responsive AIEgen could become a valuable tool in the clinic for the diagnosis and treatment of ALP-related cancers.

Declaration of competing interest

The authors declare that they have no known competing financial interests or personal relationships that could have appeared to influence the work reported in this paper.

Acknowledgments

This work was supported by Natural Science Foundation of Jilin Province (No. SKL202302002). Key Research and Development project of Jilin Provincial Science and Technology Department (No. 20210204142YY). The Science and Technology Development Program of Jilin Province (No. 2020122256JC). Beijing Kechuang Medical Development Foundation Fund of China (No. KC2023-JX-0186-BQ079). Talent Reserve Program (TRP), the First Hospital of Jilin University (No. JDYY-TRP-2024007).

Supplementary materials

Supplementary material associated with this article can be found, in the online version, at doi:10.1016/j.cclet.2024.109765.

References

[1] B.S. Wang, S.D. Zhang, J.X. Meng, et al., Adv. Mater. 33 (2021) 2103999.
[2] Z.H. Ding, C.J. Wu, G.C. Chu, et al., Nature 470 (2011) 269–273.
[3] T.T. Wheeler, P. Cao, M.D. Ghouri, et al., Sci. China Chem. 65 (2022) 1498–1514.
[4] Z. Wang, A.N. Liu, X.C. Li, et al., Talanta 256 (2023) 124255.
[5] Z.M. Wang, L.N. Chen, C.S. Huang, Y.K. Huang, N.Q. Jia, J. Mater. Chem. B 5 (2017) 3498–3510.
[6] Y.L. Lin, Y.Q. Zhao, Z. Yang, et al., Talanta 241 (2022) 123241.
[7] A.D. Salaam, P.T.J. Hwang, A. Poonawalla, et al., Nanotechnology 25 (2014) 425103.
[8] K.X. Huang, B. Shi, W.G. Xu, et al., Acta Biomater. 27 (2015) 179–193.
[9] P. Armanetti, A. Chilla, F. Margheri, et al., Adv. Sci. 8 (2021) 2001175.
[10] J.W. Wang, J.J. Fu, H. Chen, et al., Biosens. Bioelectron. 224 (2023) 115051.
[11] L.A. Austin, B. Kang, M.A. El-Sayed, Nano Today 10 (2015) 542–558.
[12] Y.X. Liu, M.D. Cao, Z.X. Huang, et al., Chin. Chem. Lett. 33 (2022) 1855–1860.
[13] J.Y. Zhu, A. Ouyang, Z.L. Shen, et al., Chin. Chem. Lett. 33 (2022) 1907–1912.
[14] M.Z. Lv, M.X. Chen, R. Zhang, et al., Cell Res. 30 (2020) 966–979.
[15] X.H. Lin, R. Zhu, Z.Z. Hong, et al., Adv. Funct. Mater. 31 (2021) 2101278.
[16] D. Huo, S. Liu, C. Zhang, et al., ACS Nano 11 (2017) 10159–10174.
[17] E.M. Higbee-Dempsey, A. Amirshaghaghi, M.J. Case, et al., J. Am. Chem. Soc. 142 (2020) 7783–7794.
[18] Z. Wang, D.Z. Wang, X.J. Ren, et al., ACS Cent. Sci. 9 (2023) 1976–1988.
[19] F. Danhier, J. Control Release 244 (2016) 108–121.
[20] D.Y. Liu, L.Y. Liu, F.Y. Liu, et al., Adv. Sci. 8 (2021) 2100074.
[21] R.R. Wang, N.N. Zhao, F.J. Xu, Adv. Funct. Mater. 27 (2017) 1700256.
[22] Q.L. Mao, J. Fang, A.N. Wang, et al., Angew. Chem. Int. Ed. 60 (2021) 23805–23811.
[23] M.Q. Liu, M. Yang, X.Z. Wan, et al., Adv. Mater. 35 (2023) 2208995.
[24] J.L. Shen, B. Situ, X.C. Du, et al., ACS Sens. 7 (2022) 766–774.
[25] Y.Y. Yuan, C.J. Zhang, M. Gao, et al., Angew. Chem. Int. Ed. 54 (2015) 1780–1786.
[26] Y.Q. Xu, M.Y. Cui, W.C. Zhang, et al., Chem. Eng. J. 428 (2022) 132514.
[27] C.F. Wu, R. Zhang, W. Du, L. Cheng, G.L. Liang, Nano Lett. 18 (2018) 7749–7754.
[28] D.F. Yao, S.Y. Yang, Y.S. Wang, et al., Nanoscale 11 (2019) 6307–6314.
[29] J.Z. Liu, H.M. Meng, L. Zhang, et al., Chin. Chem. Lett. 32 (2021) 3421–3425.
[30] Z. Feng, H. Wang, X. Chen, B. Xu, J. Am. Chem. Soc. 139 (2017) 15377–15384.
[31] S.Y. Yang, D.F. Yao, Y.S. Wang, et al., Chem. Commun. 54 (2018) 9841–9844.
[32] R.C. Guo, X.H. Zhang, P.S. Fan, et al., Angew. Chem. Int. Ed. 60 (2021) 25128–25134.
[33] Z. Wang, X.L. Ou, L. Guan, et al., Biosens. Bioelectron. 235 (2023) 115386.
[34] Z. Wang, H.Y. Xing, A.N. Liu, et al., Acta Biomater. 166 (2023) 581–592.
[35] Z. Zhao, H.K. Zhang, J.W.Y. Lam, B.Z. Tang, Angew. Chem. Int. Ed. 59 (2020) 9888–9907.
[36] S. Suzuki, S. Sasaki, A.S. Sairi, et al., Angew. Chem. Int. Ed. 59 (2020) 9856–9867.
[37] B.N. Wang, L.R. Wang, H.Z. Wu, et al., Bioact. Mater. 23 (2023) 223–233.
[38] H.L. Zhao, N. Li, C.X. Ma, et al., Chin. Chem. Lett. 34 (2023) 107699.